

## Article

# Cu-Y<sub>2</sub>O<sub>3</sub> Catalyst Derived from Cu<sub>2</sub>Y<sub>2</sub>O<sub>5</sub> Perovskite for Water Gas Shift Reaction: The Effect of Reduction Temperature

Zeyu Wang<sup>1,2</sup>, Fengying Luo<sup>1,2</sup>, Nan Wang<sup>1</sup> and Xinjun Li<sup>1,\*</sup>

<sup>1</sup> Guangzhou Institute of Energy Conversion, Chinese Academy of Sciences, Guangzhou 510640, China; wangzy1@ms.giec.ac.cn (Z.W.); luofy@ms.giec.ac.cn (F.L.); wangnan@ms.giec.ac.cn (N.W.)

<sup>2</sup> University of Chinese Academy of Sciences, Beijing 100049, China

\* Correspondence: lixj@ms.giec.ac.cn

**Abstract:** Cu<sub>2</sub>Y<sub>2</sub>O<sub>5</sub> perovskite was reduced at different temperatures under H<sub>2</sub> atmosphere to prepare two Cu-Y<sub>2</sub>O<sub>3</sub> catalysts. The results of the activity test indicated that the Cu-Y<sub>2</sub>O<sub>3</sub> catalyst after H<sub>2</sub>-reduction at 500 °C (RCYO-500) exhibited the best performance in the temperature range from 100 to 180 °C for water gas shift (WGS) reaction, with a CO conversion of 57.30% and H<sub>2</sub> production of 30.67 μmol·g<sub>cat</sub><sup>-1</sup>·min<sup>-1</sup> at 160 °C and a gas hourly space velocity (GHSV) of 6000 mL·g<sub>cat</sub><sup>-1</sup>·h<sup>-1</sup>. The catalyst reduced at 320 °C (RCYO-320) performed best at the temperature range from 180 to 250 °C, which achieved 86.44% CO conversion and 54.73 μmol·g<sub>cat</sub><sup>-1</sup>·min<sup>-1</sup> H<sub>2</sub> production at 250 °C. Both of the Cu-Y<sub>2</sub>O<sub>3</sub> catalysts had similar structures including Cu<sup>0</sup>, Cu<sup>+</sup>, oxygen vacancies (Vo) on the Cu<sup>0</sup>-Cu<sup>+</sup> interface and Y<sub>2</sub>O<sub>3</sub> support. RCYO-500, with a mainly exposed Cu<sup>0</sup> (100) facet, was active in the low-temperature WGS reaction, while the WGS activity of RCYO-320, which mainly exposed the Cu<sup>0</sup> (111) facet, was greatly enhanced above 180 °C. Different Cu<sup>0</sup> facets have different abilities to absorb H<sub>2</sub>O and then dissociate it to form hydroxyl groups, which is the main step affecting the catalytic rate of the WGS reaction.



**Citation:** Wang, Z.; Luo, F.; Wang, N.; Li, X. Cu-Y<sub>2</sub>O<sub>3</sub> Catalyst Derived from Cu<sub>2</sub>Y<sub>2</sub>O<sub>5</sub> Perovskite for Water Gas Shift Reaction: The Effect of Reduction Temperature. *Catalysts* **2022**, *12*, 481. <https://doi.org/10.3390/catal12050481>

Academic Editors: Maria Luisa Di Gioia, Luisa Margarida Martins and Isidro M. Pastor

Received: 1 April 2022

Accepted: 23 April 2022

Published: 25 April 2022

**Publisher's Note:** MDPI stays neutral with regard to jurisdictional claims in published maps and institutional affiliations.



**Copyright:** © 2022 by the authors. Licensee MDPI, Basel, Switzerland. This article is an open access article distributed under the terms and conditions of the Creative Commons Attribution (CC BY) license (<https://creativecommons.org/licenses/by/4.0/>).

**Keywords:** Cu<sub>2</sub>Y<sub>2</sub>O<sub>5</sub> perovskite; reduction temperature; Cu-Y<sub>2</sub>O<sub>3</sub> catalyst; water gas shift reaction; Cu<sup>0</sup> facet

## 1. Introduction

The water gas shift (WGS) reaction is considered to be a promising method for CO conversion and H<sub>2</sub>/CO modulation [1], which is of great significance to the subsequent synthesis of chemical products and the electrical power generation of fuel cells [2,3]. As we all know, the WGS reaction (CO + H<sub>2</sub>O ↔ CO<sub>2</sub> + H<sub>2</sub>) is an exothermic reaction [4] and the conversion decreases with the reaction equilibrium thermodynamically limited as the temperature increases [5]; more attention is being paid to the research of a low-temperature WGS reaction.

The catalysts currently used in the low-temperature WGS reaction mainly include noble metal catalysts such as Pt, Au [6,7], etc., as active components and Cu-based catalysts. However, noble metals catalysts are relatively expensive and not suitable for large-scale application in industrial production. Cu as an active component is considered to have good activity in low temperature WGS reaction. [8]. The effect of Cu doping on the activity of Fe<sub>3</sub>O<sub>4</sub> on the WGS reaction based on the DFT calculation indicated that Cu species could strengthen the CO absorption, slow down active site inactivation and improve Fe ion activity, which are beneficial to WGS reaction at lower temperatures [9]. Jeong et al. prepared Cu-CeO<sub>2</sub> with varying Cu loading, which suggested that a further increase in Cu loading (>80 wt%) resulted in a reduction of CO conversion under the same conditions and the catalytic performance decreased with an increasing reaction temperature as the Cu loading exceeded 50% [10]. The CeO<sub>2</sub>/Cu catalyst with Cu/Ce ratio of 9:1 via an aerosol-spray method maintained a stable and best WGS reaction rate of 17 μmol·g<sup>-1</sup>·s<sup>-1</sup>

at 250 °C for 50 h, which showed that optimal CeO<sub>2</sub> coverage on Cu surface was about 20% and an increase or decrease in Cu proportion led to a catalytic performance decrease [11].

In previous studies, in addition to the Cu content and Cu chemical state affecting the performance, different Cu<sup>0</sup> exposed facets affected the catalytic activity of WGS reaction. Jiang et al. studied the absorption of H, OH and H<sub>2</sub>O on the oxygen-preadsorbed Cu<sup>0</sup> (111), Cu<sup>0</sup> (100) and Cu<sup>0</sup> (110) surfaces, which indicated that the surface reactivity for the WGS reaction was in the order of Cu<sup>0</sup> (110) > Cu<sup>0</sup> (100) > Cu<sup>0</sup> (111) [12]. Mudiyansele et al. concluded that the dominant WGS pathway on Cu<sup>0</sup> (111) was the redox reaction and Cu<sup>0</sup> (111) readily absorbed and dissociated H<sub>2</sub>O to transform into OH species [13]. Muller et al. suggested that Cu<sup>0</sup> (100) easily absorbed hydrogen(H\*) while Cu<sup>0</sup> (110) was easily covered with absorbed CO\* [14]. Li et al. investigated the mechanism of Cu<sup>0</sup> (111), Cu<sup>0</sup> (100) and Cu<sup>0</sup> (211) for WGS reaction by DFT calculation, which showed the activation barrier of reaction steps: Cu<sup>0</sup> (211) < Cu<sup>0</sup> (100) < Cu<sup>0</sup> (111) [15]. Therefore, it is necessary to explore the effect of Cu<sup>0</sup> facets on the catalyst surface.

Different reduction temperatures will cause the samples to achieve different degrees of reduction, resulting in different structures. Furthermore, the growth of crystal facets on the catalyst surface is affected by the reduction temperature. In this paper, the Cu<sub>2</sub>Y<sub>2</sub>O<sub>5</sub> perovskite sample was prepared by the sol-gel method, which was further reduced at 320 °C and 500 °C, respectively. The physicochemical characterizations and WGS reaction of two reduced catalysts were carried out. The probable mechanism of the effect of different reduction temperatures of catalysts on WGS performance was discussed.

## 2. Results

The essential information of the three prepared samples are shown in Table 1. Three samples had same Cu content and the two reduced catalysts were derived from the CYO.

**Table 1.** The essential information of samples.

Sample	Cu Content (%)	Perovskite Calcinated	Reduction Condition
CYO	33.02	650 °C-3 h + 850 °C-5 h	-
RCYO-320	33.02	650 °C-3 h + 850 °C-5 h	320 °C-4 h(8% H <sub>2</sub> /Ar)
RCYO-500	33.02	650 °C-3 h + 850 °C-5 h	500 °C-4 h(8% H <sub>2</sub> /Ar)

### 2.1. Characterization of the Samples

XRD patterns of CYO sample and the reduced catalysts are shown in Figure 1. The CYO sample showed single Cu<sub>2</sub>Y<sub>2</sub>O<sub>5</sub> perovskite structure, which was related to the orthorhombic Cu<sub>2</sub>Y<sub>2</sub>O<sub>5</sub> perovskite structure (PDF-83-0341) [16]. The XRD patterns of the two reduced catalysts were completely inconsistent with that of the CYO sample. The diffraction peaks of orthorhombic Cu<sub>2</sub>Y<sub>2</sub>O<sub>5</sub> perovskite had totally disappeared and transformed into Y<sub>2</sub>O<sub>3</sub> support and Cu<sup>0</sup> in RCYO-320 and RCYO-500 catalysts. The 2θ values of 20.50, 29.15, 33.78, 35.90, 39.84, 43.47, 48.83, 53.20, 56.17, 57.61, 59.03, 60.43, 71.06, 72.33 and 74.86° (PDF-43-1036) corresponded to the cubic Y<sub>2</sub>O<sub>3</sub> structure [17]. The cubic Cu<sup>0</sup> peaks are present at 2θ values of 43.30, 50.43 and 74.13° (PDF-04-0836) [18]. These results suggested that no structure of the Cu<sub>2</sub>Y<sub>2</sub>O<sub>5</sub> perovskite existed in the RCYO-320 and RCYO-500 catalysts but Cu<sup>0</sup> particles and Y<sub>2</sub>O<sub>3</sub> support. However, with the increase of the reduction temperature, the characteristic peaks of Cu<sup>0</sup> particles and Y<sub>2</sub>O<sub>3</sub> formed became sharper in the end, which indicated that the crystal structures of Cu<sup>0</sup> particles and Y<sub>2</sub>O<sub>3</sub> were more regular after reduction at high temperature. The crystallite size of reduced catalysts derived from Cu<sub>2</sub>Y<sub>2</sub>O<sub>5</sub> perovskite was calculated by the well-known Scherrer formula [19]:

$$D = K\lambda/\beta \cos \theta \quad (1)$$

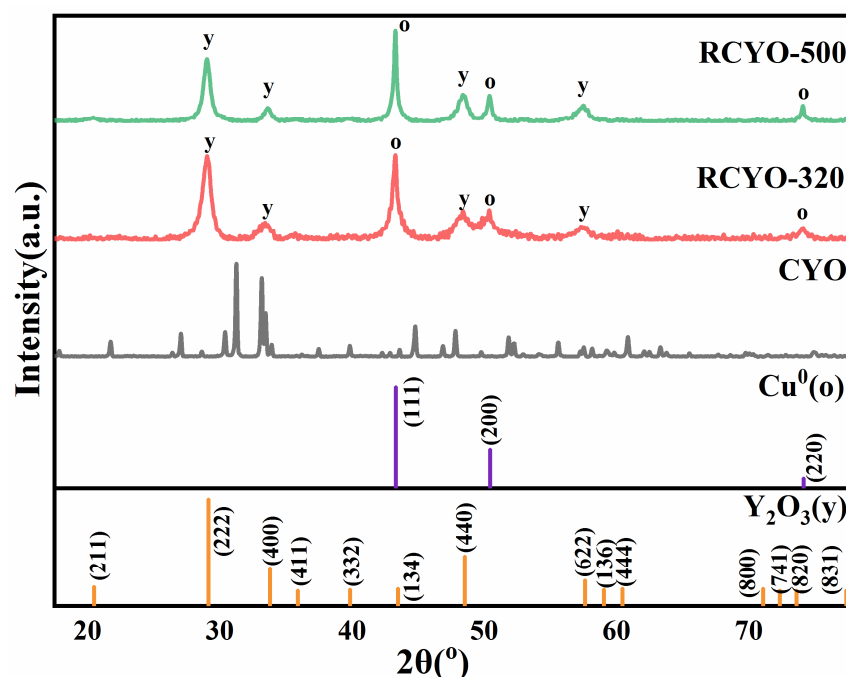


**Figure 1.** The XRD patterns of crystalline sample of CYO and reduced samples of RCYO-320 and RCYO-500.

In this equation, the  $D$  is crystallite size,  $K$  is Scherer constant = 0.89,  $\lambda$  is Cu  $K\alpha$  wavelength of 0.15406 nm,  $\theta$  is angle and  $\beta$  is FWHM.

The crystallite size of  $\text{Cu}^0$  particles in RCYO-320 and RCYO-500 catalysts were 17.07 nm and 24.35 nm, respectively. Both Cu-based catalysts had small  $\text{Cu}^0$  particles, which would exhibit good performance for WGS reaction.

As shown in Table 2, the total pore volume and surface area of RCYO-320 and RCYO-500 are displayed.

**Table 2.** Total pore volume and surface area of the two reduced catalysts.

Sample	Total Pore Volume ( $\text{cc}\cdot\text{g}^{-1}$ )	Surface Area ( $\text{m}^2\cdot\text{g}^{-1}$ )
RCYO-320	$5.786 \times 10^{-2}$	87.316
RCYO-500	$8.221 \times 10^{-2}$	97.614

The total pore volume and surface area of RCYO-320 were  $5.786 \cdot 10^{-2} \text{ cc}\cdot\text{g}^{-1}$  and  $87.316 \text{ m}^2\cdot\text{g}^{-1}$ . The parameters of RCYO-500 were slightly higher than RCYO-320, which included total pore volume of  $8.221 \cdot 10^{-2} \text{ cc}\cdot\text{g}^{-1}$  and surface area of  $97.614 \text{ m}^2\cdot\text{g}^{-1}$ . This slight difference may be related to the degree of sintering and pore formation of the catalyst during reduction. When the specific surface area of the catalyst was larger, the probability of the active site being in contact with the reaction gas was greater, which would help to improve the activity of the WGS reaction [20]. The nitrogen adsorption-desorption isotherms and the corresponding pore-size distribution of two catalysts are shown in Figure 2. Figure 2a shows the pore-size distribution of the two catalysts and the pore diameters were mainly distributed at 4.35 nm and 7.90 nm, indicating that both catalysts belong to mesoporous materials [21]. According to IUPAC classification, the curves in Figure 2b belonging to type III showed an H1-type hysteresis loop. In general, the H1 hysteresis ring was observed in mesoporous materials, which had small pore size and spherical particle aggregates with relatively uniform size [22]. Therefore, it was indicated that the two catalysts had the structure with uniform particle size distribution and narrow pore size distribution.

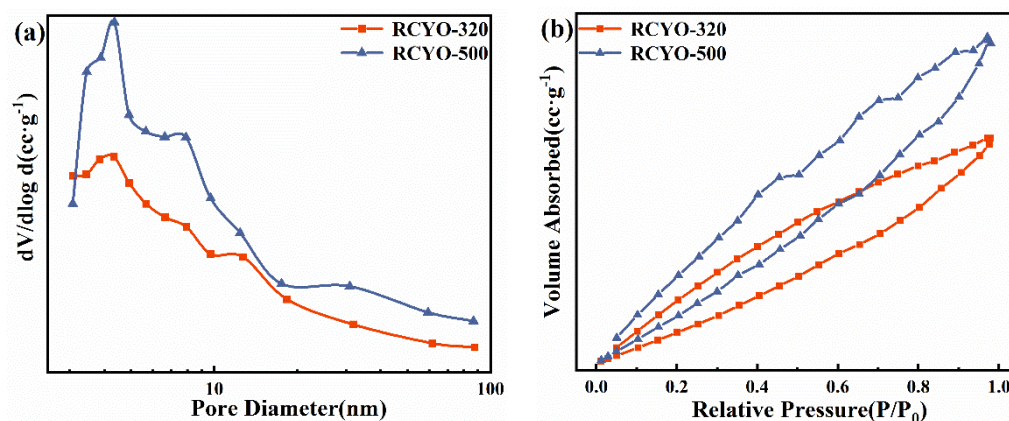


**Figure 2.** The corresponding pore-size distribution (a) and nitrogen adsorption-desorption isotherms (b) of RCYO-320 and RCYO-500 catalysts.

The  $H_2$ -TPR profiles of the crystallization of the CYO sample are shown in Figure 3.

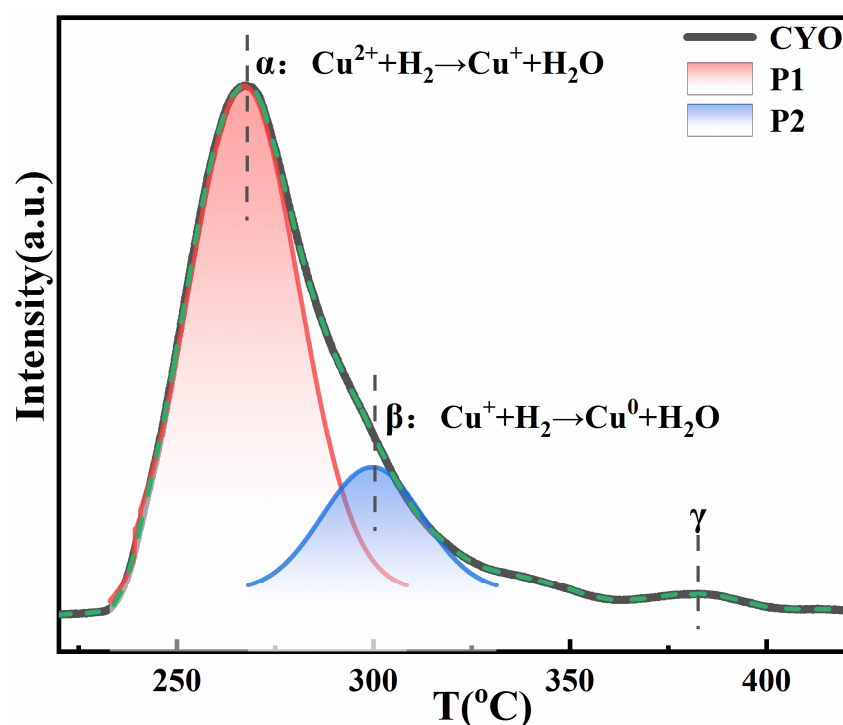


**Figure 3.**  $H_2$ -TPR profile of fresh CYO sample.

The  $H_2$ -TPR curve can be divided into two main peaks and a tiny peak. The first peak (peak  $\alpha$ ) about 267.52 °C was attributed to the reduction of  $Cu^{2+}$  in  $Cu_2Y_2O_5$  perovskite to  $Cu^+$  species. The second peak (peak  $\beta$ ) at 299.71 °C was related to the reduction of  $Cu^+$  species to metallic  $Cu^0$  state [23–26]. In addition, it can be seen from the calculation that the area ratio of peak  $\alpha$  to peak  $\beta$  was much larger than 1, which implied that there was still a certain amount of  $Cu^+$  inside the sample even after complete reduction. Therefore, a small amount of amorphous  $Cu^+$  in the interior of the reduced sample existed, which could be attributed to the strong interaction between the  $Cu^0$  particles and the support after reduction. The  $\gamma$  peak at about 370 °C was most likely due to the reduction of  $Y_2O_3$  to form  $Y_2O_{3-\delta}$ . In the preparation of the two reduced catalysts, the reduction temperatures were chosen based on the  $H_2$ -TPR profile of CYO. At 320 °C, the structure of the  $Cu_2Y_2O_5$  perovskite almost completely decomposed and collapsed into Cu species and  $Y_2O_3$ . The  $Cu_2Y_2O_5$  perovskite reduced at 500 °C can achieve a high reduction degree.

In order to explore the surface morphologies of the catalysts, Figure 4 shows the SEM and TEM images of RCYO-320 and RCYO-500 catalysts. Most of the Cu particles supported on  $Y_2O_3$  were observed in both SEM images of Figure 4a,d, which were consistent with the results of the XRD. Furthermore, with the increased reduction temperature, the phenomenon of agglomeration and growth of Cu species on the support were more obvious. TEM images of RCYO-320 were observed in Figure 4b,c, which can be found that obvious flocs were attached to the carrier, while obvious species aggregated on the support of RCYO-500 were observed in Figure 4e,f. The flocs should be the fine dendrites of reduced Cu species attached to  $Y_2O_3$  and the large black particles in RCYO-500 should correspond to the large particles of grown agglomerated Cu particles [27,28]. The SEM and TEM images were basically consistent with the results of the XRD.

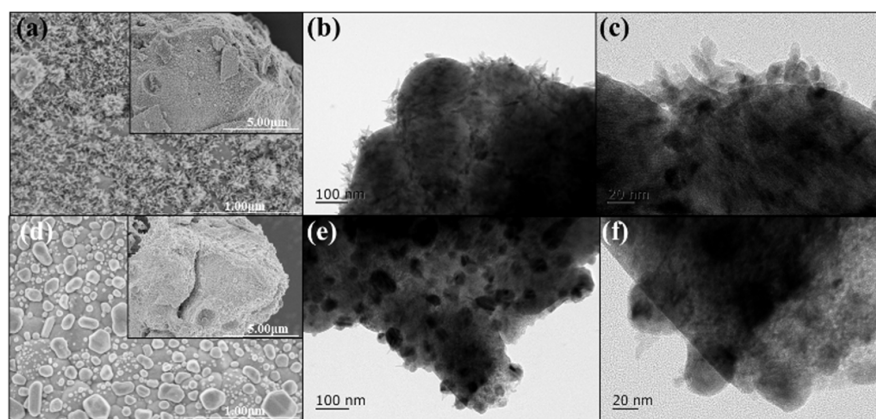


**Figure 4.** SEM images of (a) RCYO-320 and (d) RCYO-500 catalysts and TEM images of (b,c) RCYO-320 and (e,f) RCYO-500.

The energy-dispersive X-ray (EDX) spectroscopy of Cu element in two catalysts are shown in Figure 5, indicating that Cu elements were well distributed in RCYO-320. However, in Figure 5b, obvious graininess and agglomeration of Cu species appeared on RCYO-500, which demonstrated that high temperature made the Cu particles on the  $Y_2O_3$  support easy to agglomerate and develop [29].

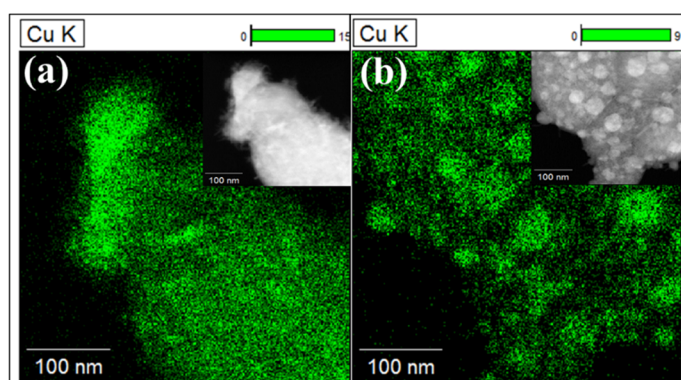


**Figure 5.** Energy-dispersive X-ray (EDX) spectroscopy of Cu element in (a) RCYO-320 and (b) RCYO-500 catalysts.

In order to explore the richer and more detailed information of the Cu species on the catalyst surface, high-resolution transmission electron microscopy (HR-TEM) were necessary to observe the surface properties of the catalysts, which are shown in Figure 6. In Figure 6a, only two groups of different crystal facets were displayed on the catalyst surface, corresponding to cubic  $Cu^{\circ}$  (111) plane and cubic  $Y_2O_3$  (222) plane [30,31] in RCYO-320, respectively. It is worth noting that there were distinct cubic  $Cu^{\circ}$  (100) and cubic  $Y_2O_3$

(222) and tiny amounts of  $\text{Cu}^\circ$  (111) [32] on RCYO-500. These results indicated that RCYO-500 had different  $\text{Cu}^\circ$  crystal facets with RCYO-320, which would lead to the catalysts exhibiting varied WGS performance. In Hansson's group, the influence of crystallographic orientation was investigated for loading along the (100), (110) or (111) direction of  $\text{Cu}^\circ$ , which may show different characteristics in the WGS reaction [33].

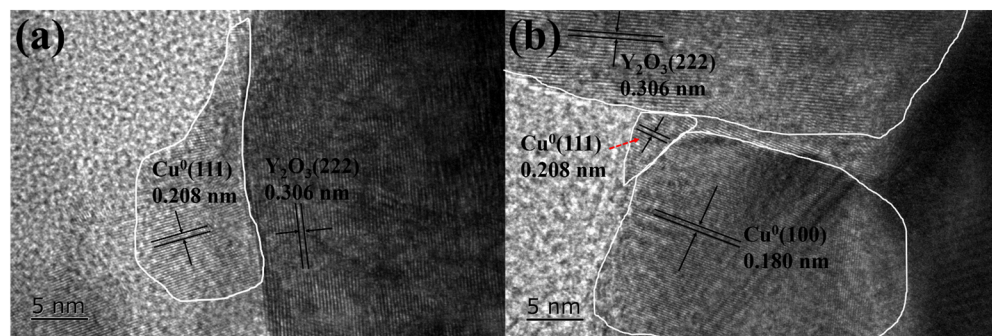


**Figure 6.** HR-TEM images of (a) RCYO-320 and (b) RCYO-500 catalysts.

To analyze the influence of the surface properties of RCYO-320 and RCYO-500 catalysts, the chemical states of O, Y and Cu elements were measured by XPS. The high resolution XPS spectra of Y 3d, O 1s, Cu 2p and Cu LMM Auger are shown in Figure 7a–d, respectively. Figure 7a shows the deconvolution results of the Y 3d XPS spectra of RCYO-320 and RCYO-500 in which four distinguishable peaks with the binding energies from 154–162 eV were obtained. The peak around 156.48 eV can be allocated to the bond of  $\text{Y}_2\text{O}_3$  3d<sub>5/2</sub> (indicated in orange) and the peak located at around 158.20 eV was assigned to the bond of  $\text{Y}_2\text{O}_3$  3d<sub>3/2</sub> (indicated in green). The peaks of  $\text{Y-CO}_3^{2-}$  3d<sub>5/2</sub> and 3d<sub>3/2</sub> were represented by blue and purple curves, located around 157.50 eV and 159.32 eV, respectively [34–36]. Combined with the XRD pattern,  $\text{Y}_2\text{O}_3$  was the main component as support. Since  $\text{Y}_2\text{O}_3$  absorbed  $\text{H}_2\text{O}$  and  $\text{CO}_2$  relatively easily, the presence of  $\text{Y-CO}_3^{2-}$  peaks was also reasonable [37].

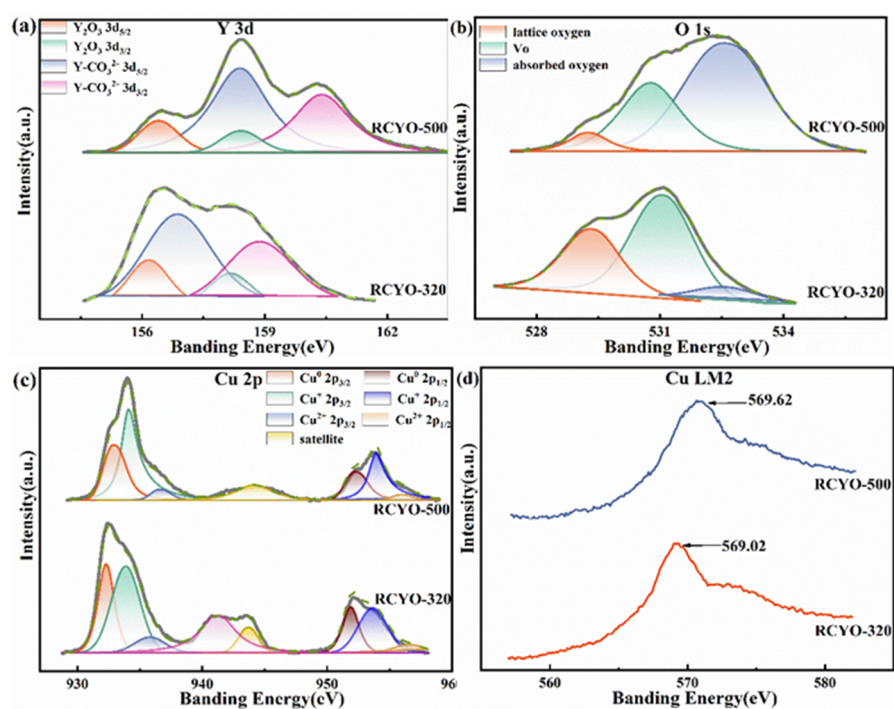


**Figure 7.** XPS binding energies for RCYO-320 and RCYO-500 catalysts: (a) Y 3d spectra, (b) O 1s spectra, (c) Cu 2p spectra and (d) Cu LMM Auger spectra.

The O 1s core level scans are shown in Figure 7b. Three distinct peaks can be detected in all XPS spectra of O 1s of catalysts. The one peak with the binding energy around 529.50 eV can be ascribed to the lattice oxygen species (indicated in orange), the second peak at about 531.00 eV can be attributed to oxygen vacancies (Vo) (in green) and the last peak located at ~533.00 eV can be assigned to adsorbed oxygen on the surface (in blue) [38,39]. By comparison, it was found that both RCYO-500 and RCYO-320 had a certain number of Vo, but there was still a large amount of adsorbed oxygen on the surface of RCYO-500, which may be related to the formation of  $Y_2O_{3-\delta}$ . The presence of  $Y_2O_{3-\delta}$  will form many Vo, resulting in spontaneous adsorption and dissociation of  $H_2O$  to form a large number of hydroxyl groups or adsorption of many  $CO_2$  covering the surface and occupying Vo, so the RCYO-500 showed a large amount of adsorbed oxygen. This indicated that RCYO-500 easily absorbed  $H_2O$  and  $CO_2$  when exposed to air and the surface oxygen was very active [40,41]. Due to the deeper reduction degree, the characteristic peaks of lattice oxygen of RCYO-500 were obviously weaker than those of RCYO-320.

The Cu 2p spectra are shown in Figure 7c. The deconvolution results can be divided into satellite peaks and three kinds of Cu 2p peaks, including  $Cu^\circ$ ,  $Cu^+$  and  $Cu^{2+}$ . The orange and wine red regions were attributed to the peaks of  $Cu^\circ$  2p<sub>3/2</sub> and 2p<sub>1/2</sub> at approximately 932.50 eV and 952.80 eV, respectively. Furthermore, the peaks of  $Cu^+$  2p<sub>3/2</sub> and 2p<sub>1/2</sub> were located around 933.90 eV and 953.80 eV, indicated in green and sapphire blue. The blue peaks (about 936.00 eV) and earthy yellow peaks (~932.70 eV) represented the 2p<sub>3/2</sub> and 2p<sub>1/2</sub> peaks of  $Cu^{2+}$  [42–44]. Figure 7d shows the Cu Auger spectra of the two catalysts, including a broad main peak around 570.00 eV. Combined with the XPS results of Cu 2p spectra, it can be confirmed that the Auger peaks of the three valence states of Cu overlap, indicating the coexistence of  $Cu^\circ$ ,  $Cu^+$  and  $Cu^{2+}$  [45].

According to the characterization results of XPS, the proportion of each valence state of Cu species was calculated, as shown in Table 3. The proportion of  $Cu^\circ$  on the surface of RCYO-320 and RCYO-500 was determined by XPS to be 34.3% and 35.8%, respectively. Furthermore, the proportion of  $Cu^+$  on the surface of RCYO-320 and RCYO-500 were 55.1% and 58.0%, respectively. Both of them had a small fraction (less than 11%) of  $Cu^{2+}$  on their surfaces. Consequently, the proportions of Cu valence states in RCYO-320 and RCYO-500 were basically similar. Both RCYO-320 and RCYO-500 showed a large amount of  $Cu^+$ , which was likely due to the strong interaction between  $Cu^\circ$  and  $Y_2O_3$ . The XPS spectrum described that both reduced catalysts formed the structures of  $Cu^\circ$  particles and Vo supported on  $Y_2O_3$  after of  $Cu_2Y_2O_5$  perovskite collapsed, which would play a vital role in the WGS reaction.

**Table 3.** Composition of surface Cu species.

Catalysts	Surface Cu Species					
	$Cu^\circ$		$Cu^+$		$Cu^{2+}$	
	B.E. (eV)	% Area	B.E. (eV)	% Area	B.E. (eV)	% Area
RCYO-320	932.30	34.3	933.87	55.1	935.80	10.6
RCYO-500	932.84	35.8	934.10	58.0	936.57	6.2

Figure 8 shows the surface species changes of RCYO-300 and RCYO-500 catalysts during the WGS reaction by in situ DRIFT test. The infrared displacement belonging to hydroxyl groups at about 1647 nm can be observed in both spectra of catalysts with increasing temperature. The areas of hydroxyl groups of RCYO-320 first increased and then remained constant above 180 °C, while the hydroxyl group areas of RCYO-500 remained unchanged with increasing temperature [46,47]. This indicated that RCYO-500 can already generate a large number of hydroxyl groups at lower temperature, which should benefit from  $Y_2O_{3-\delta}$ , which also explained that the large amount of adsorbed oxygen in the XPS results was mainly hydroxyl groups. The infrared displacement around 1540 nm and 2350 nm corresponded to carbonate species and  $CO_2$  [48]. Since no formic acid groups

and carboxyl groups were detected in the in situ drift spectra and no characteristic peak of carbonyl groups was found, the WGS catalytic mechanism of RCYO-320 and RCYO-500 can be considered as a redox process.

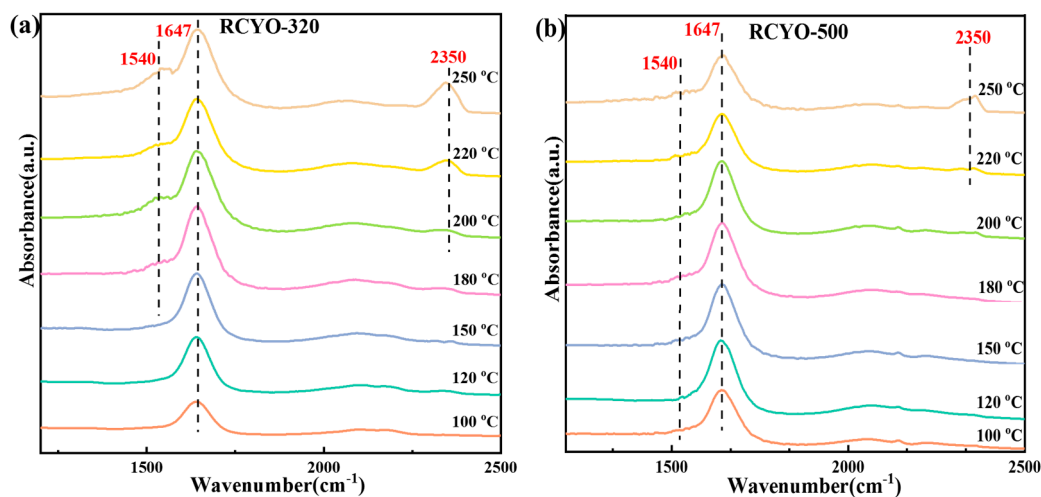


**Figure 8.** In situ DRIFT spectra of the (a) RCYO-320 and (b) RCYO-500 catalysts recorded under a simple CO + H<sub>2</sub>O (g) reaction flow.

## 2.2. Catalytic Performance Test

The WGS reaction performances of RCYO-320 and RCYO-500 at the GHSV = 6000 mL·g<sub>cat</sub><sup>-1</sup>·h<sup>-1</sup> and temperature range from 100 °C to 250 °C are shown in Figure 9a,b.

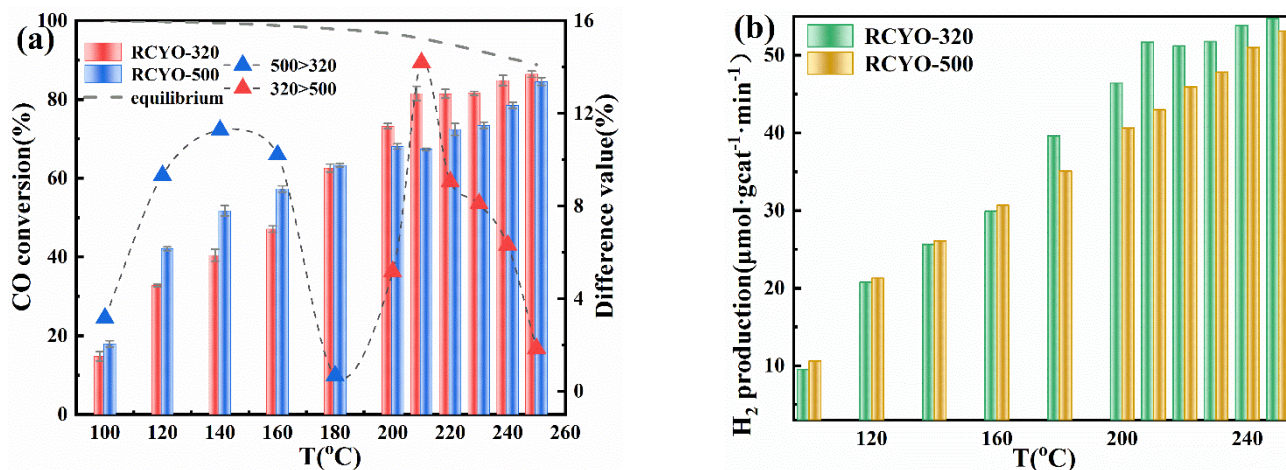


**Figure 9.** Catalytic performance diagram of (a) CO conversion and (b) H<sub>2</sub> production of two catalysts for WGS reaction when GHSV = 6000 mL·g<sub>cat</sub><sup>-1</sup>·h<sup>-1</sup> in 100–250 °C.

CO conversion and H<sub>2</sub> production were used to evaluate the catalytic activity of WGS reaction. Importantly, RCYO-320 and RCYO-500 catalysts exhibited different changes in the rate of increase in catalytic performance between 100 °C and 250 °C. Before 180 °C, the RCYO-500 exhibited better catalytic performance than RCYO-320 achieving a CO conversion of 59.30% and a H<sub>2</sub> production of 30.67 μmol·g<sub>cat</sub><sup>-1</sup>·min<sup>-1</sup>, while RCYO-320 presented 47.09% CO conversion and 29.87 μmol·g<sub>cat</sub><sup>-1</sup>·min<sup>-1</sup> H<sub>2</sub> production at 160 °C. However, when the temperature exceeded 180 °C, CO conversion and H<sub>2</sub> production of RCYO-320 increased rapidly and exceeded the values of RCYO-500. At 250 °C, RCYO-320 and RCYO-500 achieved the CO conversion of 86.44 and 84.59% and their H<sub>2</sub> production were 54.73 and 53.11 μmol·g<sub>cat</sub><sup>-1</sup>·min<sup>-1</sup>, respectively, which were basically consistent with the thermodynamic calculation results [49–51]. The change law of H<sub>2</sub> production

was basically consistent with that of CO conversion, but RCYO-320 can achieve high H<sub>2</sub> production even in low CO conversion, which implied that the structure of RCYO-320 would improve the selectivity of production. Moreover, the CO conversion of RCYO-320 began to approach equilibrium conversion at 210 °C and finally reached equilibrium at 250 °C. When the temperature was raised, the catalytic activity of RCYO-320 did not increase significantly, while the CO conversion and H<sub>2</sub> production of RCYO-500 increased rapidly with temperature increase. Consequently, RCYO-500 showed best performance on low-temperature WGS reaction and RCYO-320 performed best on high-temperature WGS reaction.

### 3. Discussion

In this work, two Cu-based catalysts derived from Cu<sub>2</sub>Y<sub>2</sub>O<sub>5</sub> perovskite were carried out WGS reaction test and structural characterizations. The XRD and SEM results confirmed that the structures of the two catalysts were Cu species supported on Y<sub>2</sub>O<sub>3</sub>, which implied that RCYO-320 had a similar structure to RCYO-500. They also had similar specific surface area and total pore volume in BET results. Furthermore, RCYO-320 had an amount of Vo on the Cu<sup>0</sup>-Cu<sup>+</sup> interface, Cu<sup>0</sup>, Cu<sup>+</sup> and Cu<sup>2+</sup> nearly as much as that of RCYO-500, which were found in the XPS spectra. It is worth noting that RCYO-320 and RCYO-500 exhibited different catalytic properties on WGS reaction, which was most likely due to differences in the Cu species formed on the surface.

The TEM images and EDX results indicated that the Y<sub>2</sub>O<sub>3</sub> supports of the two catalysts were loaded with uniformly distributed Cu<sup>0</sup> particles and the Cu<sup>0</sup> particle size of RCYO-500 was slightly larger. In the HR-TEM images, a few Cu<sup>0</sup> (111) and abundant Cu<sup>0</sup> (100) facets were found in RCYO-500, while in RCYO-320 only plentiful Cu<sup>0</sup> (111) facets could be seen. This is because the crystal will always more easily expose the crystal facets with lower surface energy during the growth process [52]. For face-centered cubic crystal, usually  $\gamma(111) < \gamma(100) < \gamma(110)$ , so the (111) facet is more likely to be revealed preferentially [53]. Due to the higher reduction temperature of RCYO-500, the surface Cu<sup>0</sup> agglomerated and exposed more (100) facets, while the Cu<sup>0</sup> (100) on the surface of RCYO-320 basically did not exist. The XPS spectra showed that on the surface of RCYO-500 existed a large amount of absorbed oxygen, while the surface of RCYO-320 had little, which indicated that RCYO-500 had a strong ability to adsorb H<sub>2</sub>O at room temperature and found it easier to dissociate H<sub>2</sub>O to form a large number of hydroxyl groups on the surface.

Since formate species, carboxyl species and carbonylic species were not found in the in situ DRIFT test, it can be determined that the two catalysts conducted the WGS reaction by the redox process [54]. After CO was adsorbed by Cu<sup>0</sup>, CO combined with the active oxygen next to Cu<sup>+</sup> to form CO<sub>2</sub> and desorbed to complete the oxidation process. At the same time, H<sub>2</sub>O was adsorbed by Cu<sup>0</sup> and dissociated into active hydroxyl and hydrogen with the help of Cu<sup>+</sup> and Vo, then the active hydroxyl groups were transferred from Cu<sup>0</sup> to replenish the active oxygen taken away by CO and dissociated. Active hydrogen was generated and the two active hydrogens combined to form hydrogen and then desorbed from Cu<sup>0</sup> to complete the reduction process. During these steps, the main steps affecting the WGS reaction catalytic rate are the dissociation of H<sub>2</sub>O and hydroxyl groups during the reduction process [55–57].

The reason for the better performance of RCYO-500 below 180 °C is that the crystal facet of Cu<sup>0</sup> (100) is more active at low temperature than that of Cu<sup>0</sup> (111). Zhang et al. have confirmed that the Cu crystal facet has an effect on the catalytic activity of WGS reaction via DFT calculations [58]. The Cu<sup>0</sup> (100) facet of RCYO-500 with Cu<sup>+</sup> and Vo can adsorb and dissociate H<sub>2</sub>O to generate a large number of hydroxyl groups at room temperature and can dissociate hydroxyl groups faster at low temperature, thereby increasing the catalytic reaction rate, as shown in Figure 10a [59]. In contrast, as shown in Figure 10b, the Cu<sup>0</sup> (111) crystal facet of RCYO-320 had enhanced activity above 180 °C, that is, the ability to synergistically adsorb and dissociate H<sub>2</sub>O with Cu<sup>+</sup> and Vo and dissociate hydroxyl groups, thereby accelerating the WGS reaction [60]. Combined with H<sub>2</sub>-TPR and XPS

results of RCYO-500, even at room temperature,  $Y_2O_3$  in RCYO-500 had a strong ability to adsorb  $CO_2$  to form  $Y-CO_3^{2-}$ . In the WGS reaction, with the temperature increasing (over  $180\text{ }^\circ\text{C}$ ), the ability of  $Y_2O_3$  to adsorb  $CO_2$  was greatly enhanced, so that a large amount of  $CO_2$  generated by the reaction stays on the surface of the support, which greatly inhibited the WGS reaction, resulting in the catalytic activity increasing slowly with the rising temperature.

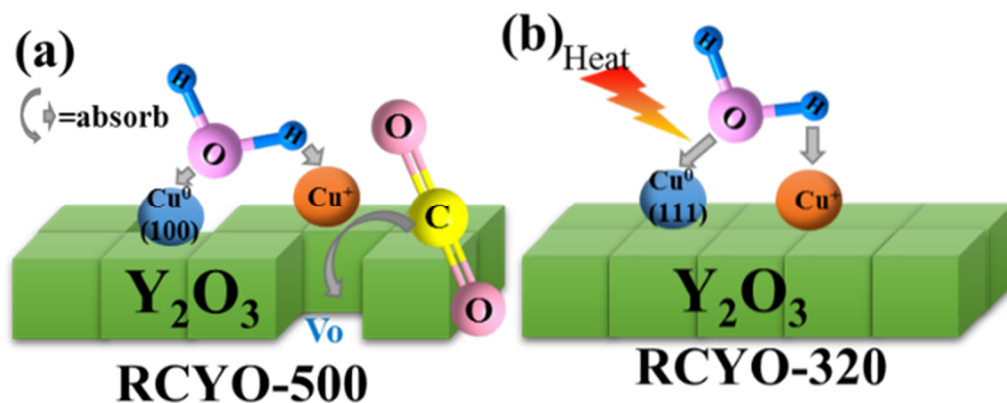


**Figure 10.** The WGS reaction mechanism diagrams of (a) RCYO-500 and (b) RCYO-320 catalysts.

#### 4. Materials and Methods

##### 4.1. Catalyst Preparation

In this work,  $Cu_2Y_2O_5$  perovskite was prepared by citric acid sol–gel method: a certain amount of yttrium nitrate hexahydrate and cupric nitrate were dissolved in deionized water and then added into a certain amount of citric acid under stirring to form an aqueous solution. The mixed solution was heated at  $80\text{ }^\circ\text{C}$  and dried at  $110\text{ }^\circ\text{C}$  overnight to obtain a dry foam-structured precursor. The precursor was subsequently calcined in a muffle furnace at  $650\text{ }^\circ\text{C}$  in 3 h and then  $850\text{ }^\circ\text{C}$  in 5 h. The obtained sample was named CYO.

Measured samples of 0.3 g of CYO were reduced in a tube furnace for 4 h under 8%  $H_2/Ar$  atmosphere with a flow of  $10\text{ mL}\cdot\text{min}^{-1}$  at different temperatures of  $320\text{ }^\circ\text{C}$  and  $500\text{ }^\circ\text{C}$ , which were denoted as RCYO-320 and RCYO-500, respectively.

##### 4.2. Catalyst Characterization

Powder X-ray diffraction (XRD) pattern was recorded using a PaNalytical X'Pert Pro diffractometer with  $Cu\ K\alpha$  radiation source operated at 40 kV and 40 mA. X-ray photoelectron spectroscopy (XPS) was determined using a Thermo ESCALAB 250XI with monochromatized  $Al\ K\alpha$  source (1486.6 eV). The C 1s line was taken as an internal standard at 284.8 eV. Surface area and porosity were analyzed by nitrogen absorption-desorption isotherm using a SI-MP-10/Pore Master 33 instrument (Quantachrome, Boynton, FL, USA) after the samples were degassed in a vacuum at  $300\text{ }^\circ\text{C}$  for 18 h. Both the pore volume and pore-size distribution were calculated through Barrett–Joyner–Hollander (BJH) method. Hydrogen temperature-programmed reduction ( $H_2$ -TPR) was performed using a mixture gas of 10 vol.%  $H_2/Ar$  ( $v/v$ ) with a flow of  $50\text{ mL}\cdot\text{min}^{-1}$ . About 40 mg of sample was heated from room temperature to  $800\text{ }^\circ\text{C}$  at a heating rate of  $10\text{ }^\circ\text{C}\cdot\text{min}^{-1}$ . The scanning electron microscope (SEM) test was performed on a Hitachi SU-70 Thermal Field Emission Scanning Electron Microscope (Analytical SEM, Hitach, Japan). The morphology of the active components on the surface of the catalysts was observed on the JEM-2100F (JEOL, Japan) transmission electron microscope (TEM). Before testing, the sample was ground finely and dispersed in ethanol solution to form a suspension. A drop was suspended on a carbon-coated copper mesh/ultra-thin carbon film until the ethanol evaporated. Mapping and high resolution were distinguished and analyzed. In situ diffuse reflectance infrared Fourier transform (in situ DRIFT) tests were performed by a FTIR spectrometer (Nicolet 6700-Q5) equipped with a MCT detector and a diffuse reflection accessory including a

temperature controllable reaction cell. The catalysts were exposed to the reaction gas in order to collect the DRIFT spectra. All in situ DRIFT spectra were recorded from 100 °C to 250 °C by accumulating 32 scans at a spectrum resolution of 4 cm<sup>-1</sup>.

#### 4.3. Catalyst Performance Test

Under atmospheric pressure, 100 mg of catalyst was placed in a fixed-bed quartz tube reactor ( $\varphi = 10$  mm) and the temperature from 100 °C to 250 °C was measured and controlled by a thermocouple. Reactant gas consisting of 3% CO/3% H<sub>2</sub>O balanced by Ar was generated by passing 3% CO/Ar through a 25 °C water-bath, with a total flux of 10 mL·min<sup>-1</sup> at the GHSV of 6000 mL·g<sub>cat</sub><sup>-1</sup>·h<sup>-1</sup>. The feed gas and reaction products were analyzed online by an online GC-2010 Shimadzu gas chromatograph and the estimated error of the gas component was within 3%.

### 5. Conclusions

In summary, two Cu/Y<sub>2</sub>O<sub>3</sub> catalysts were obtained by the reduction of Cu<sub>2</sub>Y<sub>2</sub>O<sub>5</sub> perovskite at 320 °C and 500 °C, respectively. The two catalysts mainly exposed different crystal facets of Cu<sup>0</sup>, showing different WGS catalytic performances. RCYO-500, which mainly exposed Cu<sup>0</sup> (100) facet, exhibited better WGS activity below 180 °C, achieving CO conversion of 59.30% and H<sub>2</sub> production of 30.67  $\mu\text{mol}\cdot\text{g}_{\text{cat}}^{-1}\cdot\text{min}^{-1}$  at 160 °C at the GHSV of 6000 mL·g<sub>cat</sub><sup>-1</sup>·h<sup>-1</sup>. In contrast, RCYO-320 with mainly exposed Cu<sup>0</sup> (111) facet performed well over 180 °C and reached a CO conversion of 86.44% and H<sub>2</sub> production of 54.73  $\mu\text{mol}\cdot\text{g}_{\text{cat}}^{-1}\cdot\text{min}^{-1}$  at 250 °C. The different catalytic properties are related to the Cu<sup>0</sup> crystal facets formed on the catalyst surface. The Cu<sup>0</sup> (100) of RCYO-500 with Cu<sup>+</sup> and Vo can adsorb and dissociate H<sub>2</sub>O, respectively, generating a large number of hydroxyl groups at room temperature and dissociating hydroxyl groups faster at low temperature. The Cu<sup>0</sup> (111) crystal facet of RCYO-320 cooperated with Cu<sup>+</sup> and Vo to adsorb and dissociate H<sub>2</sub>O and the dissociation ability of hydroxyl groups above 180 °C was also greatly enhanced. This finding provides ideas for the subsequent design of Cu-based catalysts for low-temperature WGS reaction.

**Author Contributions:** Formal analysis and investigation, Z.W.; writing—original draft preparation, Z.W. and F.L.; writing—review and editing, N.W.; supervision, X.L. All authors have read and agreed to the published version of the manuscript.

**Funding:** This work was financially supported by the National Key R&D Program of China (2021YFC1910404), Natural Science Foundation of Guangdong Province, China (Grant number 2021A1515010445), Science and Technology Program of Guangzhou, China (Grant number 202102020402).

**Data Availability Statement:** Not applicable.

**Conflicts of Interest:** The authors declared there are no conflict of interest.

### References

1. Poggio-Fraccari, E.; Abele, A.; Zitta, N.; Francesconi, J.; Marino, F. CO removal for hydrogen purification via Water Gas Shift and COPROX reactions with monolithic catalysts. *Fuel* **2022**, *310*, 122419. [[CrossRef](#)]
2. Wang, Y.; Diaz, D.F.R.; Chen, K.S.; Wang, Z.; Adroher, X.C. Materials, technological status, and fundamentals of PEM fuel cells—A review. *Mater. Today* **2020**, *32*, 178–203. [[CrossRef](#)]
3. Palma, V.; Goodall, R.; Thompson, A.; Ruocco, C.; Renda, S.; Leach, R.; Martino, M. Ceria-coated replicated aluminium sponges as catalysts for the CO-water gas shift process. *Int. J. Hydrogen Energy* **2021**, *46*, 12158–12168. [[CrossRef](#)]
4. Trimm, D.L. Minimisation of carbon monoxide in a hydrogen stream for fuel cell application. *Appl. Catal. A Gen.* **2005**, *296*, 1–11. [[CrossRef](#)]
5. Plama, V.; Ruocco, C.; Cortses, M.; Renda, S.; Meloni, E.; Festa, G.; Martino, M. Platinum Based Catalysts in the Water Gas Shift Reaction: Recent Advances. *Metals* **2020**, *10*, 866. [[CrossRef](#)]
6. Li, Y.; Li, X.; Zhu, B.; Zhu, A. Boosting low-temperature water gas shift reaction over Au/TiO<sub>2</sub> nanocatalyst activated by oxygen plasma. *Chem. Eng. J.* **2021**, *430*, 133013. [[CrossRef](#)]
7. Mandapaka, R.; Madras, G. Zinc and platinum co-doped ceria for WGS and CO oxidation. *Appl. Catal. B Environ.* **2017**, *211*, 137–147. [[CrossRef](#)]

8. Ma, L.; Han, D.; Ma, H.; Liu, L.; Guo, H. Characterization of Highly Dispersed Rod- and Particle-Shaped CuFe<sub>19</sub>O<sub>x</sub> Catalysts and Their Shape Effects on WGS. *Catalysts* **2019**, *8*, 635. [[CrossRef](#)]
9. Fu, Z.; Wang, J.; Zhang, N.; An, Y.; Yang, Z. Effect of Cu doping on the catalytic activity of Fe<sub>3</sub>O<sub>4</sub> in water-gas shift reactions. *Int. J. Hydrogen Energy* **2015**, *40*, 2193–2198. [[CrossRef](#)]
10. Jeong, D.W.; Na, H.S.; Shim, J.O.; Jang, W.J.; Roh, H.S.; Jung, U.H.; Yoon, W.L. Hydrogen production from low temperature WGS reaction on co-precipitated Cu-CeO<sub>2</sub> catalysts: An optimization of Cu loading. *Int. J. Hydrogen Energy* **2014**, *39*, 9135–9142. [[CrossRef](#)]
11. Yan, H.; Shao, W.P.; Cai, L.H.; Wang, W.W.; Jin, Z.; Jia, C.J. Construction of stabilized bulk-nano interfaces for highly promoted inverse CeO<sub>2</sub>/Cu catalyst. *Nat. Commun.* **2019**, *10*, 3470. [[CrossRef](#)] [[PubMed](#)]
12. Jiang, L.; Wang, G.; Cai, Z.; Pan, Y.; Zhao, X. Promotion of the water-gas shift reaction by pre-adsorbed oxygen on Cu(hkl) surfaces: A theoretical study. *Theochem J. Mol. Struct.* **2004**, *710*, 97–104. [[CrossRef](#)]
13. Mudiyansele, K.; Senanayake, S.D.; Ramirez, P.J.; Kundu, S.; Baber, A.; Yang, F.; Agnoli, S.; Axnanda, S.; Liu, Z.; Hrbek, J. Intermediates Arising from the Water-Gas Shift Reaction over Cu Surfaces: From UHV to Near Atmospheric Pressures. *Top. Catal.* **2015**, *58*, 4–6. [[CrossRef](#)]
14. Muller, A.; Comas-Vives, A.; Coperet, C. Shape and Surface Morphology of Copper Nanoparticles under CO<sub>2</sub> Hydrogenation Conditions from First Principles. *J. Phys. Chem. C* **2021**, *125*, 396–409. [[CrossRef](#)]
15. Li, Z.; Li, N.; Wang, N.; Zhou, B.; Yin, P.; Song, B.; Yu, J.; Yang, Y. Mechanism Investigations on Water Gas Shift Reaction over Cu (111), Cu (100), and Cu (211) Surfaces. *ACS Omega* **2022**, *7*, 3514–3521. [[CrossRef](#)] [[PubMed](#)]
16. Krupa, B.R.V.; Dasgupta, A.; Ghosh, C.; Sinha, S.K. Analysis of structural transformation in nanocrystalline Y<sub>2</sub>O<sub>3</sub> during high energy ball milling. *J. Alloy. Compd.* **2022**, *900*, 163550.
17. Wang, Y.; Zhang, M.; Cao, F.; Liu, Y.; Shao, L. Interfacial stability of Cu/Cu(Ru)/Si contact system for barrier-free copper metallization. *J. Alloy. Compd.* **2011**, *509*, L180–L182. [[CrossRef](#)]
18. Reddy, C.V.; Koutavarapu, R.; Shim, J.; Cheloho, B.; Reddy, K.R. Novel g-C<sub>3</sub>N<sub>4</sub>/Cu-doped ZrO<sub>2</sub> hybrid heterostructures for efficient photocatalytic Cr(VI) photoreduction and electrochemical energy storage applications. *Chemosphere* **2022**, *295*, 133851. [[CrossRef](#)]
19. Haider, S.; Shar, S.S.; Shakir, I.; Agboola, P.O. Visible light active Cu-doped iron oxide for photocatalytic treatment of methylene blue. *Cerama. Int.* **2022**, *48*, 7605–7612. [[CrossRef](#)]
20. Shu, H.; Liu, Y.; Jia, Y. Construction of Cu-BTC by carboxylic acid organic ligand and its application in low temperature SCR denitration. *Sci. Total Environ.* **2022**, *820*, 152984.
21. Zhao, R.; Wei, X.; Chu, B.; Chen, K.; Qin, Q.; Liu, H.; Zhou, Y.; Li, B.; Dong, L. Multi-phase coexisting metal oxide derived by MOFs for the CO-SCR reaction at low temperature and in situ DRIFTS study on reaction mechanism. *Appl. Surf. Sci.* **2022**, *580*, 152277. [[CrossRef](#)]
22. Garler, V.O.; Darie, C.; Isnard, O.; Bordet, P. Synthesis and neutron powder diffraction structural analysis of oxidized delafossite YCuO<sub>2.5</sub>. *Solid State Sci.* **2006**, *8*, 457–461. [[CrossRef](#)]
23. Wang, F.; Cheng, Z.; Deng, L.; Xie, H.; Xu, B.; Jiao, Z.; Zhou, G.; Zhang, X. Role of metal Cu species on methyl laurate catalytic hydrogenation to oxygen-containing compounds. *J. Saudi Chem. Soc.* **2020**, *24*, 733–741. [[CrossRef](#)]
24. Sun, M.; Cao, Y.; Lan, L.; Zou, S.; Fang, Z.; Chen, Y. Selective Catalytic Oxidation of Ammonia to Nitrogen over Iron and Copper Bimetallic Catalysts. *Acta Phys. Chim. Sin.* **2015**, *30*, 2300–2306.
25. Shan, Y.; Shi, X.; Yan, Z.; Liu, J.; Yu, Y.; He, H. Deactivation of Cu-SSZ-13 in the presence of SO<sub>2</sub> during hydrothermal aging. *Catal. Today* **2018**, *320*, 84–90. [[CrossRef](#)]
26. Baeza, P.; Bassi, R.; Villarroel, M.; Ojeda, J.; Araya, P.; Aguila, G. Adsorption of 4,6-Dimethyldibenzothylidibenzothiophene over Cu/ZrO<sub>2</sub>. *J. Chil. Chem. Soc.* **2015**, *60*, 2817–2821. [[CrossRef](#)]
27. Sivakumar, M.; Muthukutty, B.; Chen, T.W.; Chen, S.M.; Vivekanandan, A.K.; Chen, S.H.; Hatshan, M.R.; Kumar, M. Electrochemical detection of noxious antioxidant diphenylamine in fruit samples with support of Cu@nanoporous carbon modified sensor. *Chemosphere* **2022**, *292*, 133400. [[CrossRef](#)]
28. Cao, F.; Xu, Y.; Sui, J.; Li, X.; Yang, J.; Wang, Y. Low temperature Cu/Ti/Al Ohmic contacts to p-type 4H-SiC. *J. Alloy. Compd.* **2022**, *901*, 163580. [[CrossRef](#)]
29. Swathi, S.; Yuvakkumar, R.; Kumar, P.S.; Ravi, G.; Velauthapillai, D. Polyvinylpyrrolidone-assisted novel copper antimony sulfide nanorods for highly efficient hydrogen evolution reaction. *Fuel* **2022**, *314*, 123096. [[CrossRef](#)]
30. Ge, S.; Liu, X.; Liu, J.; Liu, H.; Liu, H.; Chen, X.; Wang, G.; Chen, J.; Zhang, G.; Zhang, Y.; et al. Synthesis of Ti<sub>x</sub>Sn<sub>1-x</sub>O<sub>2</sub> mixed metal oxide for copper catalysts as high-efficiency NH<sub>3</sub> selective catalytic oxidation. *Fuel* **2022**, *314*, 123061. [[CrossRef](#)]
31. Elbakkay, M.H.; El-Dek, S.I.; Farghali, A.A.; Roubay, W.M.A.E. Highly active atomic Cu catalyst anchored on superlattice CoFe layered double hydroxide for efficient oxygen evolution electrocatalysis. *Int. J. Hydrogen Energy* **2022**, *47*, 9876–9894. [[CrossRef](#)]
32. Li, Z.; Li, H.; Geng, X.; Dai, G.; Chu, Z.; Luo, F.; Zhang, F.; Wang, Q. Sandwich-Type Electrochemical Sensor for Mucin-1 Detection Based on a Cysteine-Histidine-Cu@Cuprous Oxide Nanozyme. *ACS Appl. Nano Mater.* **2022**, *5*, 2204–2213. [[CrossRef](#)]
33. Hansson, P.; Ahadi, A.; Melin, S. Molecular dynamics modeling of metric scaling effects in nanosized Cu beams holding a grain boundary. *Theor. Appl. Fract. Mec.* **2020**, *107*, 102509. [[CrossRef](#)]
34. Zhang, C.; Ruan, D.; Tang, Z.; Lu, K.; Wang, X.; Qi, J.; Liao, Z.; Lu, T. Fabrication and luminescent properties of uranium doped Y<sub>2</sub>O<sub>3</sub> transparent ceramics by sintering aid combinations. *Opt. Mater.* **2022**, *125*, 112064. [[CrossRef](#)]

35. Asaithambi, S.; Balaji, V.; Karuppaiah, M.; Sakthivel, P.; Eswari, K.M.; Yuvakkumar, R.; Selvakumar, P.; Velauthapillai, D.; Ravi, G. The electrochemical energy storage and photocatalytic performances analysis of rare earth metal (Tb and Y) doped SnO<sub>2</sub>@CuS composites. *Adv. Powder Technol.* **2022**, *33*, 103442. [[CrossRef](#)]
36. Fox-Rabinovitch, G.; Dosbaeva, G.; Kovalev, A.; Gershman, I.; Yamamoto, K.; Locks, E.; Paiva, J.; Konovalov, E.; Veldhuis, S. Enhancement of Multi-Scale Self-Organization Processes during Inconel DA 718 Machining through the Optimization of TiAlCrSiN/TiAlCrN Bi-Nano-Multilayer Coating Characteristics. *Materials* **2022**, *15*, 1329. [[CrossRef](#)]
37. Ilieva, L.; Ivanov, I.; Petrova, P.; Munteanu, G.; Karajirova, Y.; Sobczak, J.W.; Lisowski, W.; Anghel, E.M.; Kaszukur, Z.; Tabakova, T. Effect of Y-doping on the catalytic properties of CuO/CeO<sub>2</sub> catalysts for water-gas shift reaction. *Int. J. Hydrogen Energy* **2020**, *45*, 26286. [[CrossRef](#)]
38. Zhang, H.; Li, C.; Chen, X.; Fu, H.; Chen, Y.; Ning, S.; Fujita, T.; Wei, Y.; Wang, X. Layered ammonium vanadate nanobelt as efficient adsorbents for removal of Sr<sup>2+</sup> and Cs<sup>+</sup> from contaminated water. *J. Colloid Interface Sci.* **2022**, *615*, 110–123. [[CrossRef](#)] [[PubMed](#)]
39. Xu, J.; Zeng, G.; Lin, Q.; Gu, Y.; Wang, X.; Feng, Z.; Sengupta, A. Application of 3D magnetic nanocomposites: MXene-supported Fe<sub>3</sub>O<sub>4</sub>@CS nanospheres for highly efficient adsorption and separation of dyes. *Sci. Total Environ.* **2022**, *822*, 153544. [[CrossRef](#)] [[PubMed](#)]
40. Alhassan, S.I.; Wang, H.; He, Y.; Yan, L.; Jiang, Y.; Wu, B.; Wang, T.; Gang, H.; Huang, L.; Jin, L.; et al. Fluoride remediation from on-site wastewater using optimized bauxite nanocomposite (Bx-Ce-La@500): Synthesis maximization, and mechanism of F-removal. *J. Hazard. Mater.* **2022**, *430*, 128401. [[CrossRef](#)] [[PubMed](#)]
41. Teiaira, M.M.; Santos, L.C.; Tello, A.C.M.; Almeida, P.B.; Da Silva, J.S.; Laier, L.; Gracia, L.; Teodoro, M.D.; Da Silva, L.F.; Andres, J.; et al. alpha-Ag<sub>2</sub>WO<sub>4</sub> under microwave, electron beam and femtosecond laser irradiations: Unveiling the relationship between morphology and photoluminescence emissions. *J. Alloy. Compd.* **2022**, *903*, 163840.
42. Zhang, X.; Shi, Y.; Ouyang, Q.; Zhang, X.; Zhu, C.; Zhang, X.; Chen, Y. Identification of the Intrinsic Dielectric Properties of Metal Single Atoms for Electromagnetic Wave Absorption. *Nano-Micro Lett.* **2022**, *14*, 27. [[CrossRef](#)] [[PubMed](#)]
43. Yu, D.; He, J.; Xie, T.; Xu, Q.; Li, G.; Du, L.; Huang, J.; Yang, J.; Li, W.; Wang, J. Peroxymonosulfate activation using a composite of copper and nickel oxide coated on SBA-15 for the removal of sulfonamide antibiotics. *Environ. Res.* **2022**, *206*, 112301. [[CrossRef](#)] [[PubMed](#)]
44. Lykaki, M.; Stefa, S.; Carabineiro, S.A.C.; Soria, M.A.; Madeira, L.M.; Konsolakis, M. Shape Effects of Ceria Nanoparticles on the Water-Gas Shift Performance of CuO<sub>x</sub>/CeO<sub>2</sub> Catalysts. *Catalysts* **2021**, *11*, 753. [[CrossRef](#)]
45. Lee, W.J.; Lee, Y.S.; Rha, S.K.; Lee, Y.J.; Lim, K.Y.; Chung, Y.D.; Whang, C.N. Adhesion and interface chemical reactions of Cu/polyimide and Cu/TiN by XPS. *Appl. Surf. Sci.* **2003**, *205*, 128–136. [[CrossRef](#)]
46. Wen, Y.; Zhao, S.; Yi, H.; Gao, F.; Yu, Q.; Liu, J.; Tang, T.; Tang, X. Efficient catalytic oxidation of methyl mercaptan to sulfur dioxide with NiCuFe mixed metal oxides. *Environ. Technol. Innov.* **2022**, *26*, 102252. [[CrossRef](#)]
47. Pandi, K.; Preeyanghaa, M.; Vinesh, V.; Madhavan, J.; Neppolian, B. Complete photocatalytic degradation of tetracycline by carbon doped TiO<sub>2</sub> supported with stable metal nitrate hydroxide. *Environ. Res.* **2022**, *207*, 112188. [[CrossRef](#)]
48. Jurado, L.; Garcia-Moncada, N.; Bobadilla, L.F.; Romero-Sarria, F.; Odriozola, J.A. Elucidation of Water Promoter Effect of Proton Conductor in WGS Reaction over Pt-Based Catalyst: An Operando DRIFTS Study. *Catalysts* **2020**, *10*, 841. [[CrossRef](#)]
49. Liu, P. Water-gas shift reaction on oxide/Cu(111): Rational catalyst screening from density functional theory. *J. Chem. Phys.* **2010**, *133*, 204705. [[CrossRef](#)]
50. Gunawardana, P.V.D.S.; Lee, H.C.; Kim, D.H. Performance of copper-ceria catalysts for water gas shift reaction in medium temperature range. *Int. J. Hydrogen Energy* **2009**, *34*, 1336–1341. [[CrossRef](#)]
51. Ilieva, L.; Ivanov, I.; Sobczak, J.W.; Lisowski, W.; Karashanova, D.; Kaszukur, Z.; Petrova, P.; Tabakova, T. Effect of support preparation method on water-gas shift activity of copper-based catalysts. *Int. J. Hydrogen Energy* **2021**. [[CrossRef](#)]
52. Petroski, J.M.; Wang, Z.L.; Green, T.C.; El-Sayed, M.A. Kinetically controlled growth and shape formation mechanism of platinum nanoparticles. *J. Phys. Chem. B* **1998**, *102*, 3316–3320. [[CrossRef](#)]
53. Wang, Z.L. Transmission electron microscopy of shape-controlled nanocrystals and their assemblies. *J. Phys. Chem. B* **2000**, *104*, 1153–1175. [[CrossRef](#)]
54. Shido, T.; Iwasawa, Y. Regulation of Reaction Intermediate by Reactant in the Water Gas Shift Reaction on CeO<sub>2</sub>, in Relation to Reactant-Promoted Mechanism. *J. Catal.* **1992**, *136*, 493–503. [[CrossRef](#)]
55. Zhang, Z.; Zhang, J.; Jia, A.P.; Lu, J.Q.; Huang, W.X. Morphology-Dependent CO Reduction Kinetics and Surface Copper Species Evolution of Cu<sub>2</sub>O Nanocrystals. *J. Phys. Chem. C* **2020**, *124*, 21568–21576. [[CrossRef](#)]
56. Gokhale, A.A.; Dumesic, J.A.; Mavrikakis, M. On the mechanism of low-temperature water gas shift reaction on copper. *J. Am. Chem. Soc.* **2008**, *130*, 1402–1414. [[CrossRef](#)]
57. Koryabkina, N.A.; Phatak, A.A.; Ruettinger, W.F.; Farrauto, R.J.; Ribeiro, F.H. Determination of kinetic parameters for the water-gas shift reaction on copper catalysts under realistic conditions for fuel cell applications. *J. Catal.* **2003**, *217*, 233–239. [[CrossRef](#)]
58. Zhang, Z.; Wang, S.; Song, R.; Cao, T.; Luo, L.; Chen, X.; Gao, Y.; Lu, J.; Li, W.; Huang, W. The most active Cu facet for low-temperature water gas shift reaction. *Nat. Commun.* **2017**, *8*, 488. [[CrossRef](#)]

- 
59. Baraj, E.; Ciahotny, K.; Hlincik, T. The water gas shift reaction: Catalysts and reaction mechanism. *Fuel* **2021**, *288*, 119817. [[CrossRef](#)]
  60. Chen, W.H.; Chen, C.Y. Water gas shift reaction for hydrogen production and carbon dioxide capture: A review. *Appl. Energy* **2020**, *258*, 114078. [[CrossRef](#)]